Electrical Formation Factor of Clean Sand from Laboratory Measurements and Digital Rock Physics.

By

M.A. Garba[1,2], S. Vialle[2], M. Madadi[2,3]B. Gurevich[2,] and M. Lebedev[2].

[1]Department of Geology, Gombe State University Nigeria,

[2]Exploration Geophysics, Curtin University, Australia

[3]Peter Cook Centre of Carbon Capture and Storage, The University of Melbourne, Australia

Abstract

Electrical properties of rocks are important parameters for well-log and reservoir interpretation. Laboratory measurements of such properties are time-consuming, difficult, and are impossible in some cases. Being able to compute them from 3D images of small samples will allow generating massive data in a short time, opening new avenues in applied and fundamental science. To become a reliable method, the accuracy of this technology needs to be tested. In this study, we developed a comprehensive and robust workflow with clean sand from two beaches. Electrical conductivities at 1 kHz were first carefully measured in the laboratory. A range of porosities spanning from a minimum of 0.26 to 0.33 to a maximum of 0.39 to 0.44, depending on the samples. Such range was achieved by compacting the samples in a way that reproduces natural packing of sand. Characteristic electrical formation factor versus porosity relationships were then obtain for each sand type. 3D micro-computed tomography images of each sand sample from the experimental sand pack were acquired at different resolutions. Image processing was done using global thresholding method and up to 96 sub-samples of sizes from $(200)^3$ to $(700)^3$ voxels. After segmentation, the images were used to compute the effective electrical conductivity of the sub-cubes using a Finite Element electrostatic modelling. For the samples, a good agreement between laboratory measurements and computation from digital cores was found, if the sub-cube size REV is reached that is between $(1300\mu m)^3$ and $(1820\mu m)^3$, which, with an average grain size of 160µm, is between 8 and 11 grains. Computed digital rock images of the clean sands have opened a way forward in getting the formation factor within a shortest possible time; laboratory calculations take five (5) to thirty-five (35) days as in the case of clean and shaly sands respectively, whereas, the digital tomography takes just three (3) to five (5) hours.

1 Introduction

Electrical formation factor (FF) refers to the ratio of the electrical resistivity of a saturated medium (sediment or rock) to that of the saturating fluid (Guéguen and Palciauskas, 1994). This is an important parameter in exploration geophysics as, contrary to electrical resistivity of reservoirs that is dependent on the resistivity of the saturating fluid (and hence a same type

of reservoir can exhibit high or low resistivities (Constable and Srnka, 2007;Jinguuji et al., 2007;Mitsuhata et al., 2006), formation factor is an intrinsic property of the rock, independent of fluid salinity. Measurement of formation factor in the laboratory is often difficult and time-consuming, if not impossible in some cases. Minerals forming the rock or sediment sample must reach thermodynamical and electrical equilibrium with the saturating fluid, which typically takes 4 to 6 days in a high permeability high porosity clean sandstone but may require at least 4 to 6 weeks for a tight gas sand or a low porosity rock or sediment with a high clay content. Furthermore, results are affected by current leakage problems (especially at high frequencies) or electrode polarization (emphasised at low frequencies).

Hence, computation of electrical properties from microstructural models has been investigated by several teams in the past 50 years. Various methods have been proposed, from statistical models used to reconstruct 3D porous materials e.g. (Miller, 1969;Joshi, 1974;Milton, 1982;Torquato, 1987;Adler et al., 1990;Adler et al., 1992;Yeong and Torquato, 1998) to direct measurement of a 3D structure from synchrotron and X-ray computed microtomography (XRCM) e.g. (Dunsmuir et al., 1991;Spanne et al., 1994;Arns et al., 2001;Øren and Bakke, 2002;Nakashima and Nakano, 2011;Øren et al., 2007) or laser confocal microscopy (Fredrich et al., 1995). In most of these studies using XRCM images, the numerical prediction of electrical conduction conductivity underestimates the experimental results by 30 to 100% (which leads to an overestimation of the formation factor) (Spanne et al., 1994;Schwartz et al., 1994;Auzerais et al., 1996). Several explanations have been put forward to justify such discrepancy: percolation differences between model and real material, mainly to a smaller volume sampling in the model (Adler et al., 1992;Bentz and Martys, 1994); the addition of a third phase to the traditional two-phase model (rock matrix being one phase and the saturating fluid being a second phase) that counts for the bound fluid at the grain fluid interface (Zhan and Toksoz, 2007); discretization errors and statistical fluctuations (Arns et al., 2001).

The underlying question behind the computation of electrical properties of digital porous media samples (or any other rock or transport properties) is whether the obtained numerical values are accurate One aspect of this question relates to the technology itself, namely 3D imaging, image processing and segmentation, the suitability and stability of the numerical code. These three key elements of the technology have been investigated by various teams and the most comprehensive and exhaustive study performed on the various steps of the digital rock physics workflow is the benchmark comparison from (Andrä et al., 2013b, a). As

they are using various rock types, processing and computing methods, the comparison is complex: they concluded that the computed effective rock properties are affected by segmentation processes, choice of digital sub-volume, and choice of numerical code and boundary conditions. Nonetheless, the different values obtained for the formation factor deviated at most by 23% from the midrange value (Andrä et al., 2013a). For the sphere pack sample, all computed formation factors ranged from 4.3 to 4.8.

The second aspect of this question relate to the comparison of the computed values with laboratory scale experimental data to validate the correctness of the digital rock physics workflow. However, because both experiments are done at different scale (cm scale for the laboratory and mm scale for the digital computation), and because rocks are heterogeneous at all scales, the laboratory measured and digitally computed do not have to match. Instead, trends between two properties (e.g. formation factor and porosity) computationally derived and produced in the laboratory should be in good agreement (Dvorkin et al., 2011;Andrä et al., 2013a).

In the work described in this paper, we propose a robust workflow to digitally compute electrical properties of clean (i.e. that does not contain any clay or other conductive minerals) unconsolidated porous media. We first carefully measure in the laboratory the formation factor of two beach sand samples of similar mineralogy (quartz and carbonate) but of different grain size, over a wide range of porosities obtained by compacting the sand sample: hence formation factor versus porosity trends reproducing a packing as close as possible as the one found *in*-situ were obtained. We then compute the formation factor from X-ray microtomography images using the free software finite element electrostatic code from NIST using multiple sub-samples of various sizes. To our knowledge, this is the first time that such a work is done on clean sand.

2 Materials and laboratory methods

2.1 Sample collection and preparation

The samples investigated in this paper are sand samples collected from the coastal margin of the Perth basin, Western Australia. The Perth Basin is an elongate, North-South trending trough underlying approximately 100,000 square kilometres of the Western Australian margin. Sediments were shed from the adjacent Yilgarn block. The Yarragadee and

Leederville sandstone formations are intercalated with the Tamale limestone that forms the Carbonates at the Upper Cretaceous. One sample was collected from Scarborough beach (31°53'41.97 S, 115°45'17.74 E) and one from Cottesloe beach (31°59'40.62 S, 115°45'03.70 E). All the samples are composed of quartz and carbonate, in a proportion 80%/20% (in volume), respectively, as determined from the 3-phase Watershed segmentation presented in section 3.2.2 of this manuscript. Grain size was determined by micro CT-image analysis and is between 16µm - 794µm (median 140µm) for quartz grains and 19µm - 446µm (median 168µm) for carbonates grains and 17µm - 606µm (median 159µm) for quartz and 15µm - 415µm (median 172µm) for carbonate grains for Scarborough and Cottesloe beaches, respectively. Sand samples were thoroughly washed clean with tap water to remove any plants and grass debris. Loose moist sand was then packed into the different cells used to perform the electrical resistivity measurements, then forming an initially high-porosity loose random pack; decreasing porosity in subsequent experiments was achieved by shaking the cell and using tied sticks to compact the sand: this was done in a way to achieve a packing as close as possible as the one found *in-situ*. A range of 6 different porosities were obtained for the Scarborough beach sand samples, with an initial porosity of 0.40 (loosely packed) down to 0.27 when highly packed, while 5 and 4 different porosities were obtained for the Cottesloe beach sand, depending on the geometry of the cell, with the loosely packed sample having a porosity of 0.39 and the highly packed sample having a porosity of 0.30.

Porosity was determined from the weights and densities of the sand grains and the known volumes of cells used in the experiment, as:

$$\phi = \frac{\left(V_t - m/\rho\right)}{V_t} \quad (1)$$

where ϕ is porosity, V_t is the total volume of the cell, m is the average mass of the dry sand before and after the experiment and ρ is the density of the sand grains. Grain density was measured by pycnometry and found to be equal to 2.71 g/cm^2.

2.2 Laboratory set-up and measurements

2.2.1 Experimental set-up

Two different types of cells are used in the experimental set-up that was utilised to monitor the electrical resistivities of the sand samples as a function of salinity of the saturating pore water. These two experimental set-ups are schemed in Figures 1 and 2. For the cell called
150 "flow cell", sample's electrical resistances are measured while saline solutions of increasing salinities are continuously flooded through the sand samples. Before proceeding with the next saline solution, the reading of the sample's electrical resistance is let stabilize for a few hours. For the cell called "static cell", the sand samples are successively saturated with saline solutions of increasing salinities, let equilibrate with no fluid flow until stability of the sample
155 electrical resistance reading is achieved, and then drained before saturating the sand sample with the next saline solution. Thus, the utilization of this rectangular shape "static cell" drastically reduces the experimental time, moreover the sample preparation for "static cell" is easier than for "flow cell. The flow cell is of cylindrical shape, 27 cm in length and 5 cm in radius (total volume of 2,120.6 cm^3) while the static cell is of rectangle shape, 29.8 cm in
160 length, 8.7 cm in width and 6.2 cm of height (total volume of 1,607.41 cm^3).

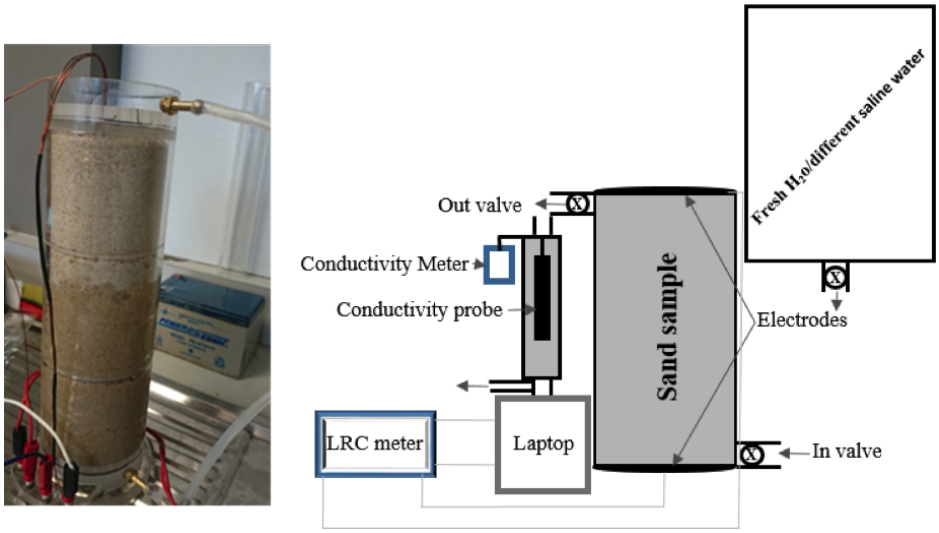

Figure 1: Photo (left) and schematic drawing (right) of the experimental set up for the flow cell.

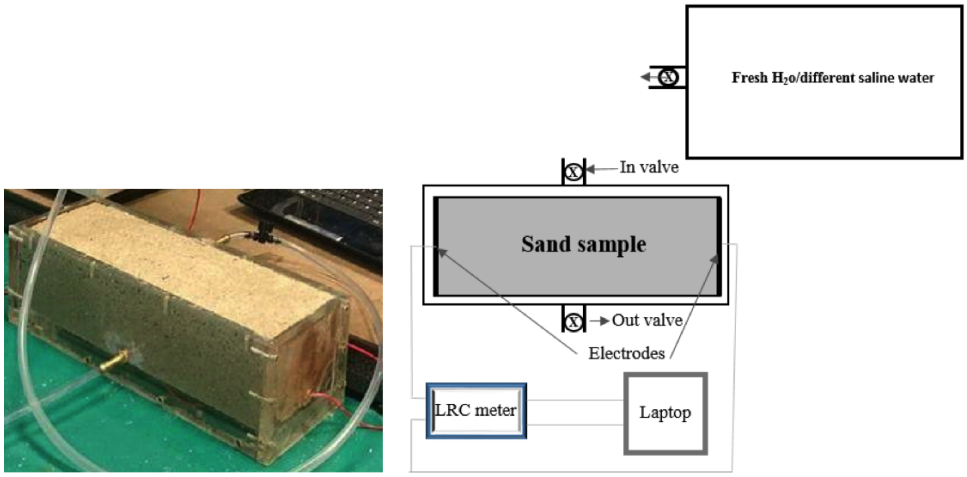

Figure 2: Photo (left) and schematic drawing (right) of the experimental set up for the static cell.

Both cells are made up of Perspex (Acrylic) and have an outlet and an inlet connected by tubing to a tank that serves as reservoir for the various solutions injected into the sand samples. The solutions flow through the sand samples via gravity (falling-head method) and, for the flow cell, two valves, at the inlet and outlet, are used to achieve a flow rate ranging from 0.52 to 2.75 ml/s. This flow rate is continuously recorded.

Injected solutions are fresh and saline solutions made with tap water and table salt in various amounts: 5 different salinities of 0g/L, 5g/L, 15g/L, 25g/L and 35g/L were made; both were measured on an electric balance (*Napco JA-5000*) and the solution was stirred until complete dissolution of the salt into water.

Both cells are equipped with two electrodes made of zinc wire gauze with surface areas of 78.55 cm^2 and 53.94 cm^2 for the dynamic and static cells, respectively. The electrodes are glued at the bottom and at the lid cover of the cylindrical dynamic cell while they are fixed on both sides of the rectangular static cell; the two electrodes of each cell are connected to a LCR meter (*Stanford research System SR720*), connected itself to a laptop to monitor the electrical resistance of the sand sample; recording time interval for the dynamic cell laboratory measurements is taken at 1 minute interval while the recording time interval for the static cell laboratory measurement is 10 minutes. A drive voltage of 1 Vrms is applied and a frequency of 1 kHz is chosen to minimize the phase angle between voltage and current (i.e. electrode polarization): with these conditions, the monitored Q factor did not exceed 0.095 indicating the system is nearly purely resistive. For the dynamic cell laboratory

measurements, the conductivity of the injected solutions coming out of the cell is monitored by an encased conductivity meter (Hanna edge) attached to the cell at intervals of 1 minute, to make it synchronous with the sand sample resistance measurements. The fluid electrical conductivity for the static cell set-up is measured with the same probe using the saturating solution drained from the sand sample once the resistance has become stable.

2.2.2 Computation of electrical formation factor

Because the sand samples do not contain any clay and because the injected solutions have a conductivity (10^{-2} to 5.0 10^{+1} S/m) much larger than that of quartz or carbonate surface conductivity (5.4 10^{-3} S/m (Miller et al., 1988), and 1.4 10^{-3} S/m (Vialle, 2008) respectively), surface and matrix electrical conductivities can be neglected (e.g. Johnson and Sen, 1988; Garrouch and Sharma, 1994); the electrical formation factor F is then given by

$$F=R_s R_w \tag{2}$$

with

$$R_s = r_s \frac{A}{L} \tag{3}$$

$$R_w = \frac{1}{\sigma_w} \tag{4}$$

where R_s is the resistivity of the sand sample saturated with water, R_w is the resistivity of the water, r_s the measured resistance of the sand sample saturated with water, A the surface area of the electrode, L the length of the cell and σ_w the measured conductivity of water.

To obtain the formation factor, the sample's resistivity, once it has stabilized, is plotted against the saline water's resistivity, and the formation factor is given by the inverse of the slope. Such as a plot is given in Figure 3 for the example of Cottesloe Beach sample with porosity 33%".

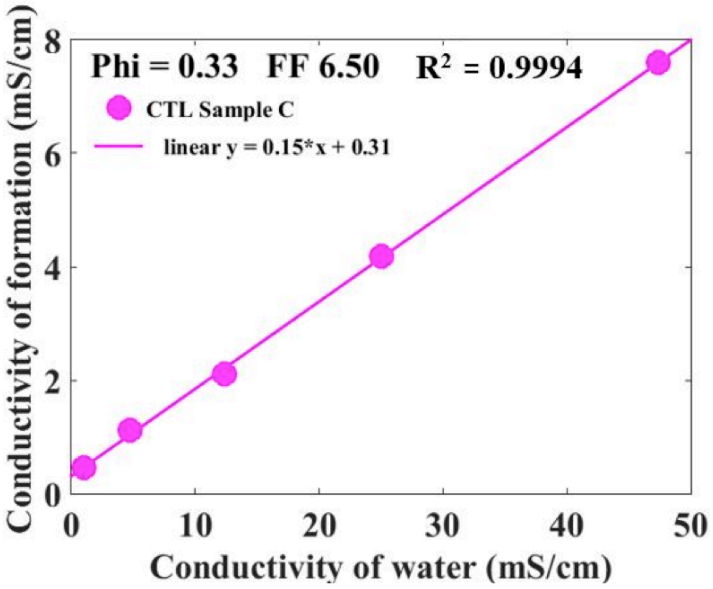

Figure 2: Sand sample conductivity as a function of water conductivity for the Cottesloe beach sample with porosity of 33%. The slope of the linear correlation gives a formation factor FF of 6.50.

3 Digital rock samples and computation of electric properties

3.1 Image acquisition

Two samples were prepared for imaging with X-Ray Micro-Computed Tomography (XRMCT), one from Scarborough beach and one from Cottesloe beach. Loose sand was put in a cylindrical Pyrex glass tube of 6 mm in diameter and 6 cm in height, and the tube was inserted in the core holder of the micro-tomograph. The samples were scanned with the 3D X-ray Microscope Versa XRM 500 (Zeiss – XRadia) using a X-ray energy of 60keV, a current of 70.66 mA and a power of 5W. In each scan 3000 projections (radiographs) were acquires. The exposure time was 2s per radiograph. Initial cone-beam 3D image reconstruction was performed using the software XM Reconstruction (XRadia). A secondary reference was required to remove geometrical artefacts during reconstruction. After 3D reconstruction, 3D volume was sliced onto 2D images for further processing. A total number of 1021 2D images for Scarborough beach sample and 991 2D images for Cottesloe beach were available for analysis. Total scanning time was 2hrs 55minutes and 2hrs 42minutes for Scarborough and Cottesloe samples respectively. A nominal voxel sizes of $(2.5761\mu m)^3$ and

230 $(2.5516\mu m)^3$ was achieved with a source-to-sample and detector-to-sample distances of 11mm and 22mm, for both Scarborough and Cottesloe beach samples respectively.

3.2 Image processing

3.2.1 Image filtering

We used the software package Avizofire 9 (FEI Visualization Sciences Group) for image
235 enhancement and segmentation. Grey-scale images of the 2D slices were processed using a non-local means filter in the intensity range of 255 – 5344 for Scarborough beach and 255 - 5467 for Cottesloe beach, with the aim of removing ring artefacts in the images and properly enhancing interfaces between the pores and grains as well as removing noise. Non-local means filter has been shown to effectively remove ring artefacts without introducing edge
240 smoothing contrary to many other filters and thus does not require the use of an additional mask (see for example the review paper of Schluter et al., 2014).

Figures 4(a)-4(d) shows raw and filtered images for both Scarborough and Cottesloe beach: we can easily notice that the quality of the image has increased. In these images, the white grains are carbonate, grey grains are quartz, while black within the cycle corresponds to void
245 space (pores).

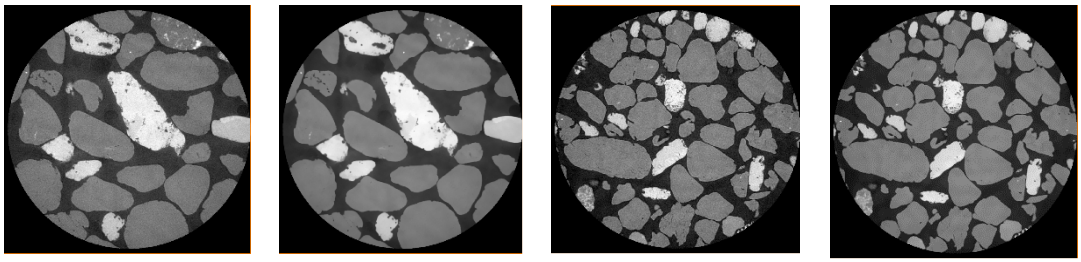

a b c d

Figure 4: a) Raw and b) filtered images of Scarborough beach sand sample; c) Raw and d) filtered images of Cottesloe beach sand sample.

3.2.2 Image segmentation

The filtered images were segmented using two types of thresholding algorithms: the first one resulted in a 2-phase segmentation that was further used for computing samples electrical conductivities; the second one is a watershed algorithm that resulted in a 2- or 3-phase

segmentation used for grain analysis. Note that filtering and segmentation workflows were applied to the full 3D dataset. Figure 5 shows the histogram for both samples.

2-phase segmentation by global thresholding

Because both quartz and carbonate have very low conductivity compared to that of water, they can be both considered as non-conductive for computation purposes of electrical conductivity of the water-saturated sand sample. Hence quartz and carbonate can be put in a single phase, and pores will constitute a second phase, that will be later on filled with a conductive fluid for the computation of sample electrical properties. We use here a global threshold segmentation algorithm to separate pores from grains: the set intensity value separating pores from grains (both quartz and carbonate grains having higher intensity values than that of pores) is kept the same for all 2D slices.

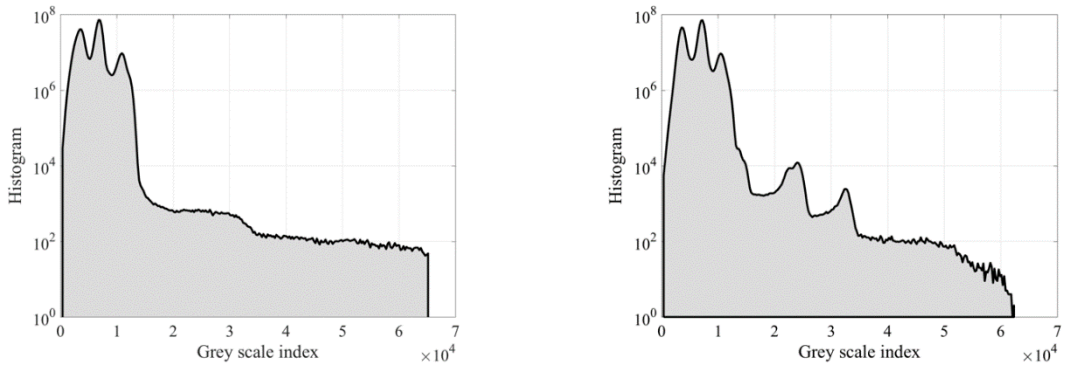

a b

Figure 5: Histogram of (a) Scarborough and (b) Cottesloe beaches.

Poor segmentation can affect accurate calculation of porosity. To check the quality of the segmentation, we compare the porosity estimated in the laboratory with the one estimated from micro CT-scan images. We made a random loose pack of sand (cm^3) in the laboratory to obtain the highest porosities of 0.361 and 0.349 from Scarborough and Cottesloe beaches respectively while the smaller scanned sample of the sand (mm^3) was also randomly packed in the small tube from which porosities of 0.369 and 0.359 were obtained from the images of Scarborough and Cottesloe beaches respectively.

Watershed segmentation

We used a marker based watershed segmentation algorithm from Avizo Fire 9. We defined either 2 or 3 marker ranges of grey scale intensity for either, pore and grains, or for pore, carbonate grains and quartz grains, respectively. We then performed a watershed flooding for each of these 2 or 3 phases. The 2-phase watershed segmentation allows computation of pore volume and grain size distribution, whereas the 3-phase segmentation (figure 6) gives volume fraction of the different minerals.

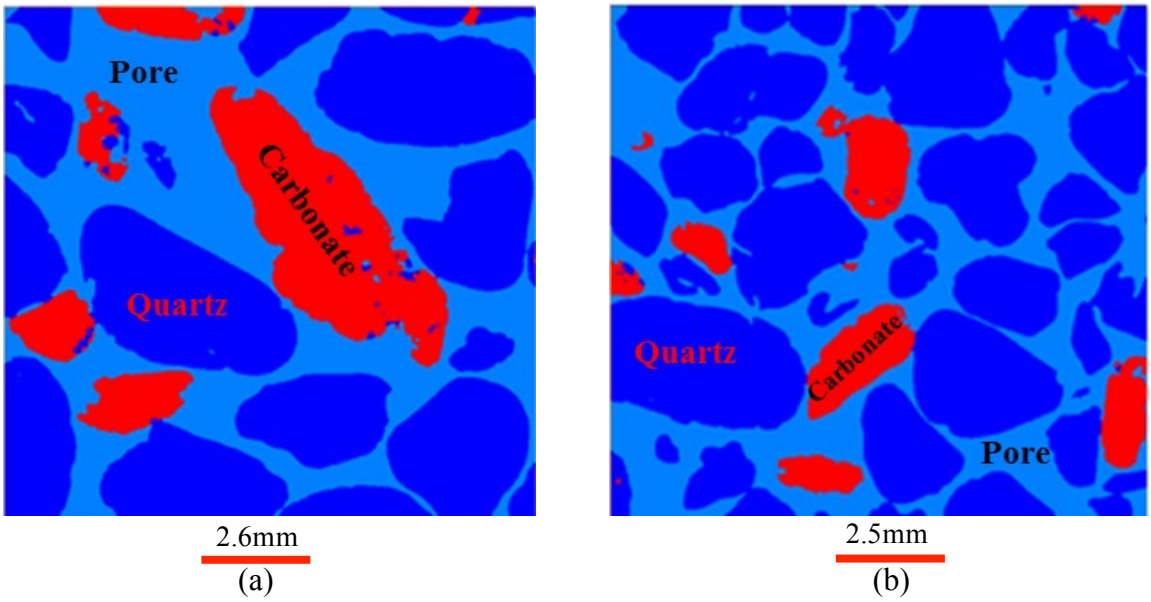

Figure 6: 3-phases watershed segmentation of the sand samples a) Scarborough; b) Cottesloe

From this segmentation, we computed the volume fraction of quartz and carbonate (excluding the pore volume). It gives 81.9% of quartz and 18,% of carbonate for Scarborough sample and 87.8% of quartz and 12.2% of carbonate for Cottesloe sample.

3.2.3 Image cropping

The 3D filtered and segmented volumes for each of the two sand samples were subdivided into overlapping sub-cubes (96 in total) of 4 different sizes: 3 sub-cubes of a size of $(700)^3$, 8 of a size of $(500)^3$, 13 of a size of $(350)^3$, and 20 of a size of $(200)^3$ for Scarborough beach sample, and 5 sub-cubes of a size of $(700)^3$, 10 of a size of $(500)^3$, 13 of a size of $(350)^3$, and 24 of a size of $(200)^3$ for Cottesloe beach sample. Porosity was estimated using Avizo software for each of these 96 sub-cubes.

The 2D cropped images were then exported in binary format for computation of electrical properties.

3.3 Computational studies of electrical fields of micro-CT images

To estimate conductivity from micro-CT images, we assume that pores are electrically conductive, and that the solid phases are not conductive. This assumption based upon the concept that mainly the ions in fluid-filling pores can be drifted under the effect of external electric fields. To estimate the conductivity from images, first, we have to calculate an average current density.

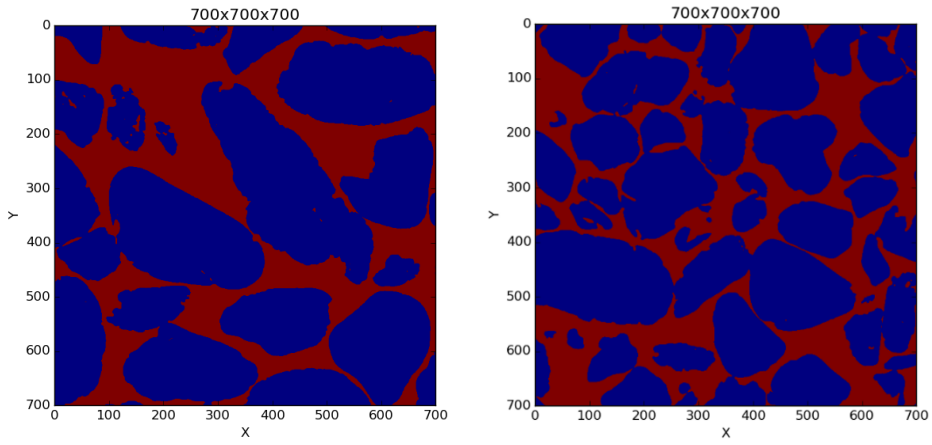

a b

Figure 7: 700 binary images (a) Scarborough and (b) Cottesloe beaches.

If we assume that the conservation of charge is valid in the pore structure, then no net charges are created or annihilated in the pore volume and pore surfaces; the current density vector obeys the following equation:

$$\nabla . J = 0. \tag{5}$$

On the other hand, Ohm's law at the microscopic level assumes that the current density is proportional to electric fields:

$$J = \sigma_w \nabla V \tag{6}$$

where J is the electrical current density, σ_w is the electrical conductivity of the fluid that fills the pore space, V is the electrical potential field (voltage). By substituting Eqn. (6) into Eqn. (5), we have the Laplace equation as:

$$\nabla \cdot \left(\sigma_w \nabla V \right) = 0 \tag{7}$$

Eqn. (7) can be solved numerically for pore structures by applying an external electric field ($\vec{E}_{ext}$ on the boundaries. One of most reliable numerical methods to estimate the average current density from 3D images is the finite element method. We use the same free software written by (Garboczi, E. J. 1998). This method, by minimizing the electrical energy stored in the porous volume under study, estimates the local potential fields (V) at each coordinate system (pore and solid phases). For a giving microstructure, because of the applied fields or other boundary conditions, the final voltage distribution is determined by minimization of the total energy stored in the system (Garboczi, E. J. 1998). Figures 7a and 7b show the potential field variations in Scarborough and Cottesloe beach samples, respectively. This can help us evaluate the effective current density ($\vec{J}_{av}$) by using equation (8) and by taking the volume average of the local current density vectors ($\vec{J}$). On the other hand, the volume average of current density is defined as:

$$\vec{J}_{av} = \langle \vec{J} \rangle = \sigma_{eff} \vec{E}_{ext} \tag{9}$$

where σ_{eff} is the effective conductivity of the porous medium. Effective conductivity is a 2nd rank tensor. In Equation (7), the current density ($\vec{J}_{av}$) and the external electrical field ($\vec{E}_{ext}$) are vectors. If we assume that the external electrical field is unidirectional (let assume in the x-direction, $\vec{E}_{ext} = E \cdot \vec{u}_x$) then the current density can have components on any other directions and can be thus written in the general form as:

$$\vec{J}_{av} = J_x \cdot \vec{u}_x + J_y \cdot \vec{u}_y + J_z \cdot \vec{u}_z \tag{10}$$

Then, from Eqn. (7), the current density can be rewritten as:

$$\vec{J}_{av} = \sigma_{xx} E \cdot \vec{u}_x + \sigma_{yx} E \cdot \vec{u}_y + \sigma_{zx} E \cdot \vec{u}_z \tag{11}$$

In homogenous media, we expect the current density to be negligible in the direction perpendicular to the external electrical fields. This implies that for homogenous media, the effective conductivity tensor is a diagonal matrix. On the other hand, for heterogeneous media, the current density in the direction perpendicular to the external electrical field is not zero, or is not small compared to the diagonal values. Hence, in general, the current density is second rank tensor of the form:

$$\sigma = \begin{pmatrix} \sigma_{xx} & \sigma_{xy} & \sigma_{xz} \\ \sigma_{yx} & \sigma_{yy} & \sigma_{yz} \\ \sigma_{zx} & \sigma_{zy} & \sigma_{zz} \end{pmatrix}. \quad (12)$$

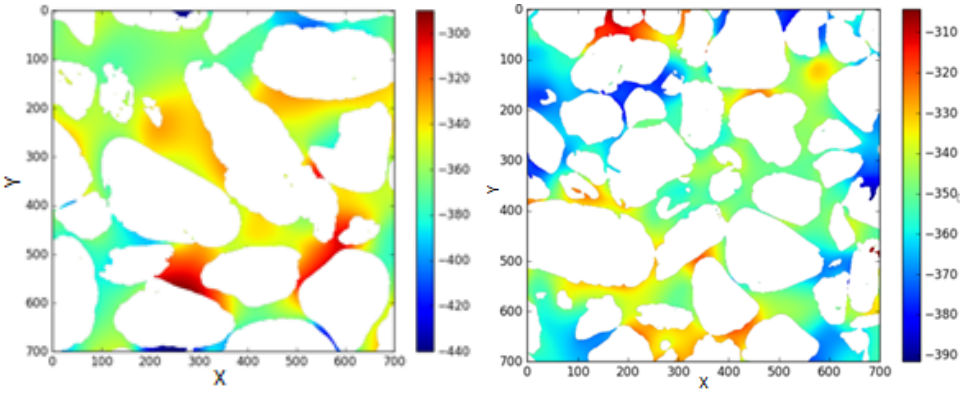

Fig 8: Electrical potential fields image output from the $(700)^3$ digital sub-cubes of (a) Scarborough (b) Cottesloe beaches. Colorbar indicates regions of high (red) and low (blue) potential field in arbitrary unit.

335

The $(700)^3$ voxel from Scarborough sample was analysed by applying a current successively in x, y and z-directions to find out whether the sample shows some anisotropy.

The output of conductivity along x, y and z-directions shows almost the same values of formation factor (5.30, 4.96 and 5.08 respectively). The difference in the values of formation
340 factor between the x-direction and y-direction is 6.6% while that between the x-direction and z-direction is 4.4%; hence, the sample presents a small anisotropy, at the scale of investigation. In the following, we took an average of the conductivities in the three different directions, which mathematically is equal to one-third of the trace of conductivity tensor; for simplicity, we then consider the conductivity as a scalar number for all images.

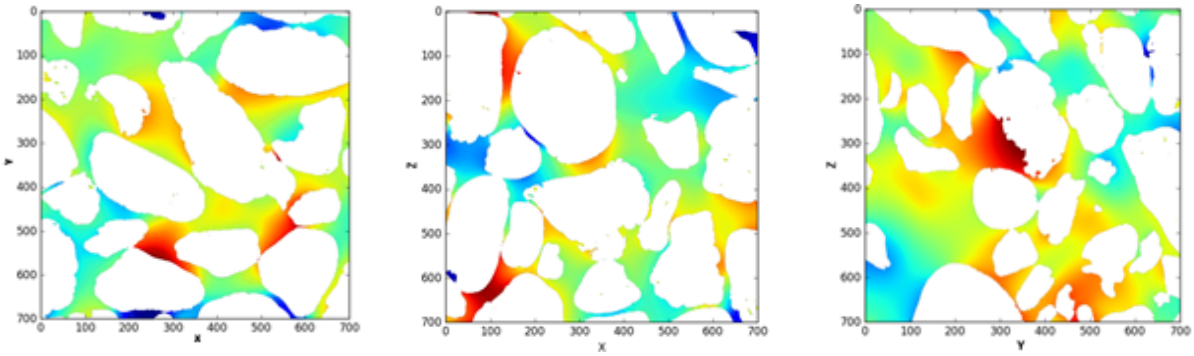

(a) (b) (c)

Figure 9: Electrical potential fields images (a) along x direction, (b) along y direction and (c) along z-axes.

345

From the effective conductivity calculated for micro-XRCT images, the electrical formation factor can be estimated as:

$$F = \frac{\sigma_w}{\sigma_{eff}}, \tag{13}$$

where σ_w is the electrical conductivity of pore fluids, taken equal to 1 in the computation. 350 Electrical formation factor is calculated for each of the different sub-cubes obtained from the micro-CT images of Scarborough and Cottesloe beach samples.

4. Results

4.1 Laboratory

355 Figure 10 displays the values of formation factor trend against porosity for Scarborough and Cottesloe beaches respectively, computed as described in section 2.2.2 and for each porosity value obtained by compacting the initial sand pack. Correlations coefficients were very good to excellent and varied between 0.975 and 0.999 and between 0.974 and 0.996 for the flow cell, for Scarborough and Cottesloe samples, respectively, and between 0.882 and 0.993 and 360 between 0.987 and 0.999 for the static cell, for Scarborough and Cottesloe samples, respectively. The results for both 'static' and 'flow' cells are reported in Tables 1 and 2 for both samples, and for all data points. The values of formation factors obtained using the

'flow' cell are higher than that obtained using the 'static' cell for both Scarborough (8.2) and Cottesloe (8.5) beach samples, whereas for Scarborough beach, formation factors have close values at high porosities and then depart from each other at lower porosities (from lower than 0.39). Some deviations between the results obtained for both static and flow cells may be due to non-uniform compaction of the samples in a case of the flow cell and or non-complete fluid replacement in the case of flow cell. In these figures, we have bounded the experimental data by two lines that represent a power-law relationship between the formation factor and porosity in the form

$$F = a \cdot \phi^{-m} = \phi^{-m} \tag{14}$$

This is Archie's law (Archie, 1942) with a tortuosity factor a of 1. Tortuosity factor usually ranges from 0.5 to 1.5, and though there has been quite a wide range reported in literature for sand, from the most used value of 0.62 (Humble formula, Winsauer et al., 1952) to up to 2.45 (Carothers and Porter, 1970). We take here the same tortuosity factor value of 1 for all samples. This is the value for clean granular formations (Sethi, 1979).

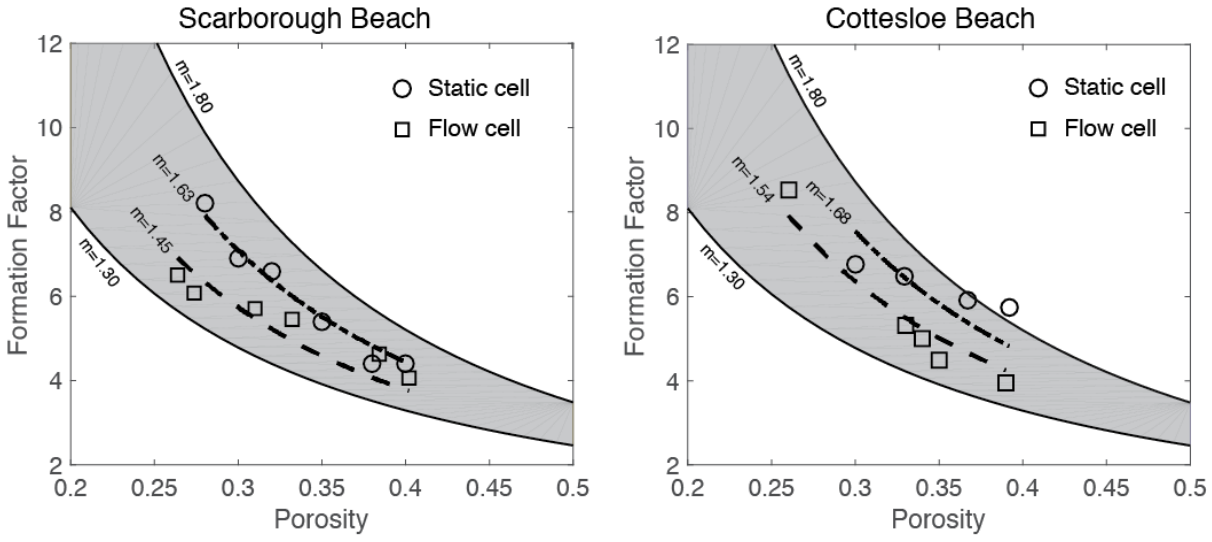

Figure 10: Laboratory measured formation factor versus porosity values for both flow and static cell for (a) Scarborough and (b) Cottesloe beach samples.

4.2 Micro CT-scan images

Formation factor were plotted against porosity for all the micro CT-scan image cubes for Scarborough and Cottesloe beaches (Figures 11 and 12, respectively).

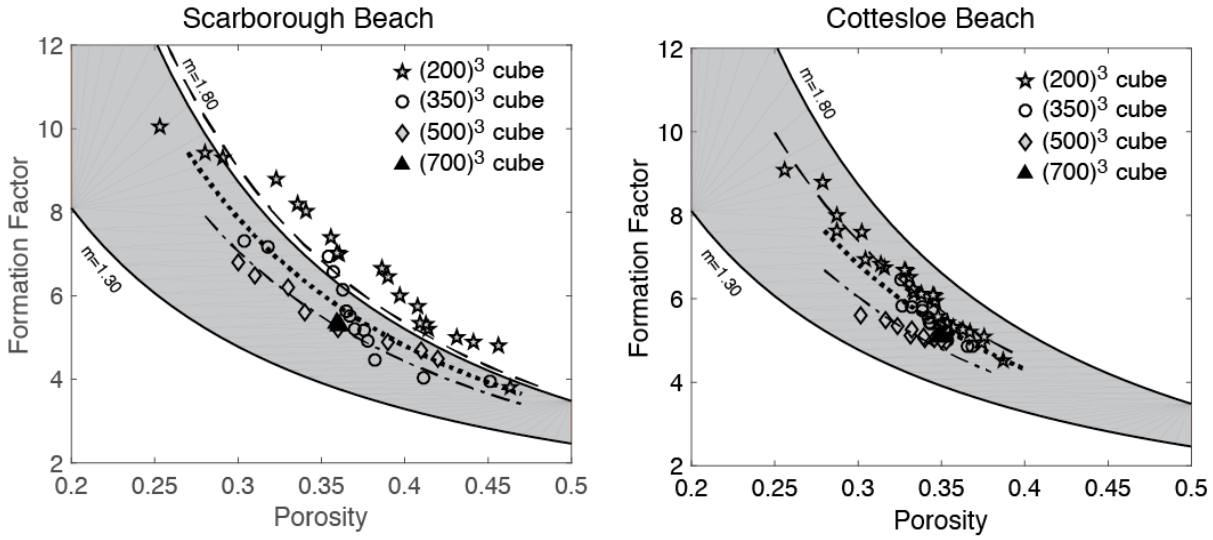

Figure 11: Formation factor against porosity for each sub-cube size of, $(200)^3$, $(350)^3$, $(500)^3$ and $(700)^3$ from both (a) Scarborough beach samples and (b) Cottesloe beach samples.

Similarly, both porosity and formation factor were plotted against the cube sizes 200^3, 350^3, 500^3 and 700^3. Scattering is shown when the cube sizes were small which begin to level off as the Representative Elemental Volume (REV) is approached. This REV is somewhere between $(500)^3$ and $(700)^3$, which corresponds to a sample size between $(1.3\text{mm})^3$ and $(1.8\text{mm})^3$.

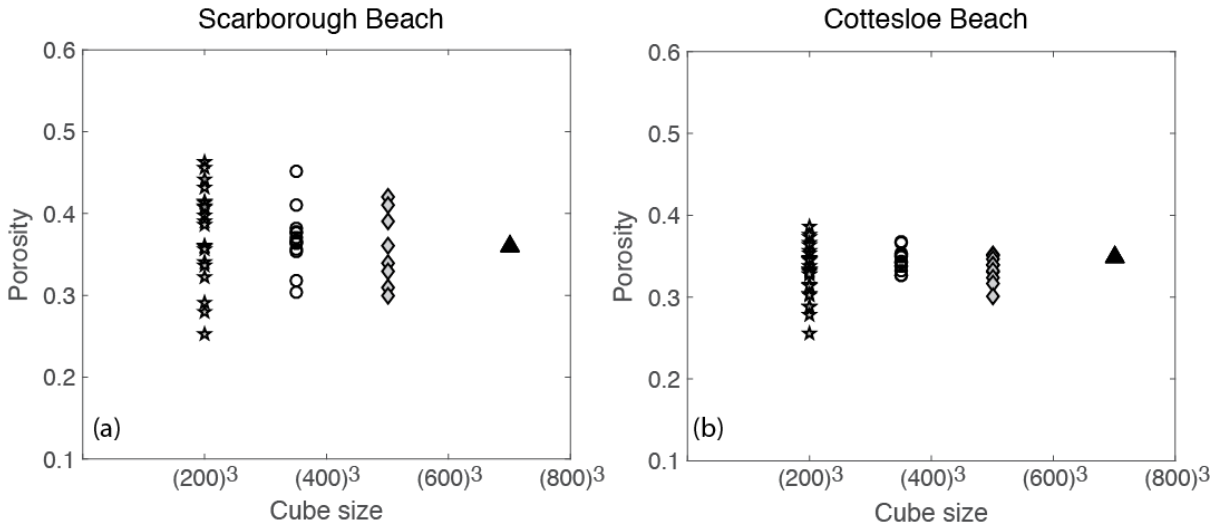

(a) (b)

Figure 12: Porosity against cube sizes (a) Scarborough beach (b) Cottesloe beach.

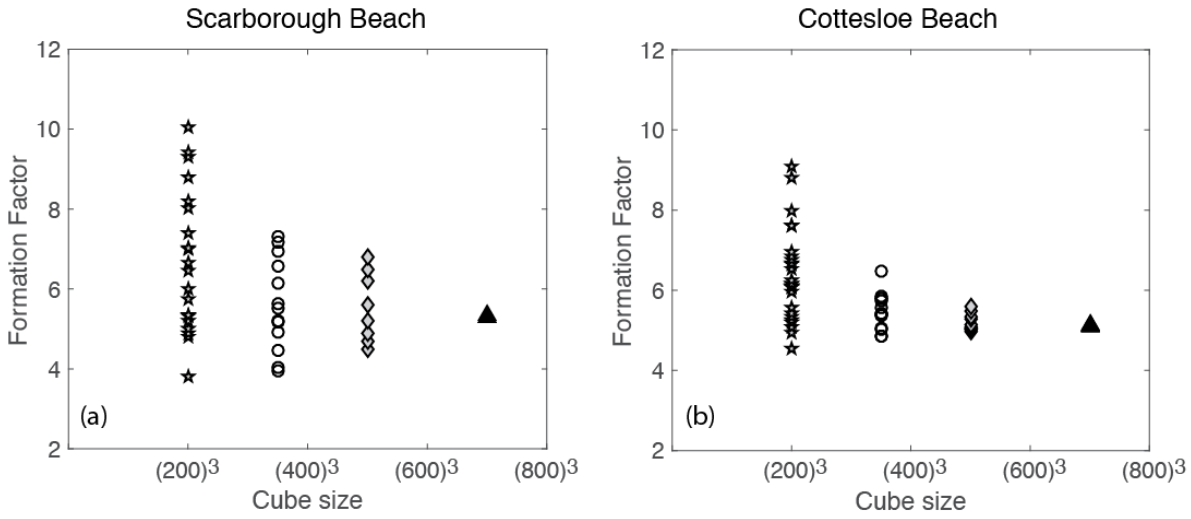

(a) (b)

Figure 13: Formation factor sizes (a) Scarborough beach (b) Cottesloe beach.

Table 1: Summary of Laboratory and micro-CT scan images result from Scarborough beach samples.

Laboratory results	Flow cell	Porosity	0.40	0.38	0.35	0.32	0.30	0.27							
		F. F	4.4	4.4	5.4	6.6	6.8	8.2							
	Static cell	Porosity	0.40	0.38	0.33	0.31	0.27	0.26							
		F. F	4.0	4.6	5.5	5.7	6.1	6.5							
Micro-CT scan images	700 cubes	Porosity	0.36	0.36	0.36										
		F. F	5.3	5.3	5.3										
	500 cubes	Porosity	0.42	0.41	0.39	0.36	0.34	0.33	0.33	0.33					
		F. F	4.5	4.7	4.9	5.2	5.6	6.2	6.5	6.8					
	350 cubes	Porosity	0.45	0.41	0.38	0.38	0.38	0.37	0.37	0.37	0.36	0.36	0.36	0.32	0.30
		F. F	3.96	4.03	4.46	4.93	5.19	5.21	5.53	5.63	6.15	6.57	6.93	7.18	7.30
	200 cubes	Porosity	0.46	0.46	0.44	0.43	0.41	0.41	0.41	0.41	0.40	0.39	0.39	0.36	0.3
		F. F	3.8	4.8	4.9	5.0	5.2	5.3	5.4	5.8	6.0	6.5	6.7	7.0	7.0
		Porosity	0.36	0.34	0.34	0.32	0.29	0.28	0.25						
		F. F	7.4	8.0	8.2	8.8	9.3	9.4	10.1						

Table 2: Summary of Laboratory and micro-CT scan images result from Cottesloe beach samples.

Laboratory results	**Flow cell**	**Porosity**	0.39	0.35	0.34	0.33	0.26								
		F. F	3.96	4.50	5.00	5.33	8.54								
	Static cell	**Porosity**	0.37	0.35	0.33	0.31									
		F. F	5.72	5.93	6.50	6.90									
Micro-CT scan images	**700 cubes**	**Porosity**	0.35	0.35	0.35	0.35	0.35								
		F. F	5.1	5.1	5.1	5.1	5.1								
	500 cubes	**Porosity**	0.35	0.35	0.34	0.34	0.34	0.33	0.33	0.33	0.32	0.30			
		F. F	4.97	5.01	5.02	5.04	5.09	5.13	5.27	5.34	5.48	5.59			
	350 cubes	**Porosity**	0.368	0.366	0.353	0.352	0.351	0.349	0.344	0.343	0.342	0.338	0.332	0.327	0.326
		F. F	4.87	4.87	5.01	5.07	5.29	5.36	5.39	5.42	5.55	5.73	5.80	5.84	6.47
	200 cubes	**Porosity**	0.39	0.37	0.37	0.36	0.36	0.35	0.35	0.35	0.35	0.34	0.34	0.33	0.33
		F. F	4.5	4.9	5.2	5.3	5.3	5.4	5.6	6.0	6.1	6.1	6.1	6.1	6.2
		Porosity	0.33	0.33	0.33	0.32	0.31	0.30	0.30	0.29	0.29	0.28	0.26		
		F. F	6.2	6.5	6.6	6.7	6.7	6.8	7.0	7.6	7.6	8.0	8.8		

5. Discussion

As noticed earlier in section 4.1, the values of formation factor obtained by the static cell are higher than that obtained by the dynamic cell (for a given porosity), for both samples. This translates in a higher cementation exponent *m*. One reason for this can be the design of the cell itself and of the way to achieve a stable reading of sample conductivity, for each fluid salinity. In the rectangular (static) cell, because the higher salinity brine is introduced or retrieved via the center of the panels (see Figure 2) there could some brine left in the corners that will only equilibrate with the new injected brine by diffusion and hence there could be a lower conductivity of the brine in these corners compared to the conductivity of the injected brine. As result the measured sample conductivity will be lowered with respect with what it should be, giving a higher ratio sample to brine conductivities (i.e. formation factor, see Eqn. 11). Using a cylindrical cell has thus the advantage of providing a better replacement of the brine.

In Figure 14 are reported data from both literature and those acquired in this study for Cottesloe and Scarborough beach samples (using the flow cell). Data from literature include natural sand samples and synthetic granular media made of plastic particles of regular geometrical shape (Wyllie and Gregory, 1953). We have bounded these data by the relationship presented in Eqn. 14, with m=1.3, which corresponds to the original work of Archie (1952) for unconsolidated media and by the same relationship, with m=1.8, for the upper bound. We see in this figure that our experimental results for Cottesloe and Scarborough beach samples are in agreement with data reported for other beach sands. Considering the data reported in this figure, we observe that Archie's classical formula for unconsolidated media underestimates the formation factor and that the departure from sphericity leads to a larger *m* coefficient. Since Archie's work, many authors have proposed alternative formation factor-porosity relationships. Winsauer et al. (1950) suggested that $a \neq 1$ in Eqn. 14 is a better expression, whereas other authors derived non-power laws dependency to porosity. From a practical point of view, no formula relating the formation factor to porosity for unconsolidated media fits all the experimental data, and, for a given porosity, the formation factor depends on the particle geometry, particle size distribution and subsequent packing.

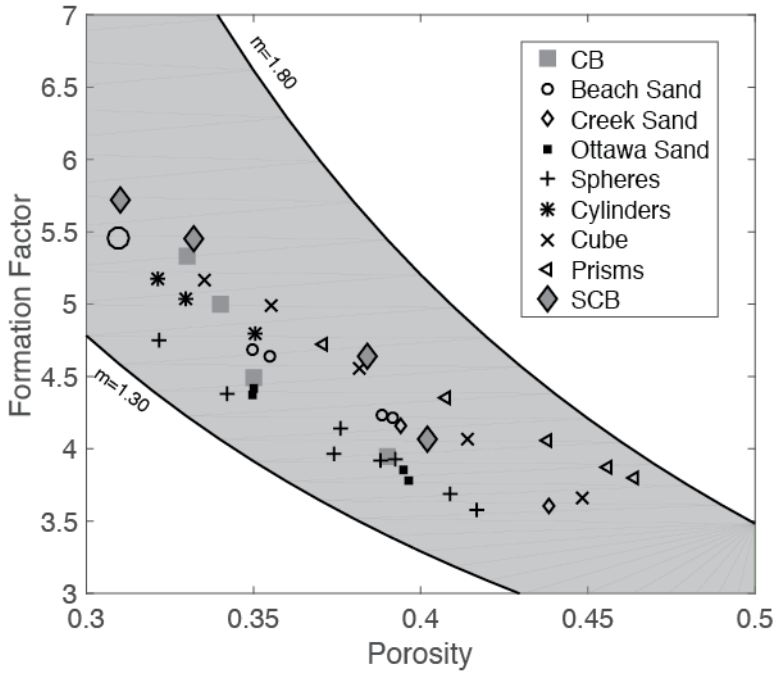

Figure14: Comparison of laboratory results with results from other workers (Wyllie and Gregory, 1953). CB stands for Cottesloe Beach samples and SCB Scarborough Beach samples.

In Figure 15, we compare laboratory data to computed data. Laboratory data are those acquired with the flow cell, which, as discussed earlier in this section, are expected to give more reliable data. Computed data are those obtained for a cube size of $(700)^3$, which is above the REV, as presented in section 4.2. We can see that there is an excellent agreement for Cottesloe beach sample, and a good agreement for Scarborough beach sample. At this stage, it is difficult to explain why one sample gave better agreement, and whether it is due to an experimental error or due to the higher content of carbonate grains for Scarborough sample that make the computation less accurate: indeed carbonate grains may present some intra-porosity (as for example micritic phases) and thus have an electrical conductivity.

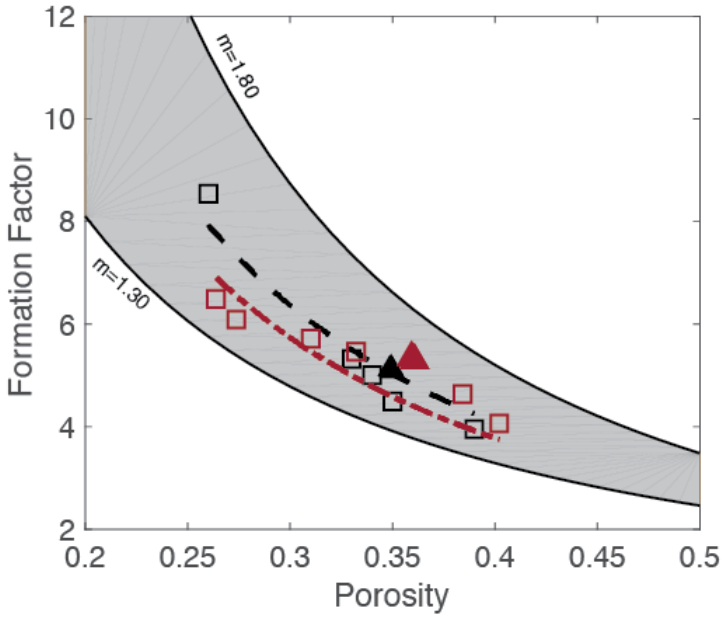

Figure 15: Comparison between laboratory results (in open symbols) end computed ones (in plain symbols). The trends in dashed lines are obtained from the laboratory-measured data.

6. Conclusions

Electrical properties of rocks are important parameters for well log and reservoir interpretation. Laboratory measurements of such properties are time-consuming, difficult, if not impossible in some cases. In view of this, we have successfully combined the scientific approach of laboratory measurements (as a bench mark) with micro-CT scan computational images and have achieved the objectives of computing the variability of computed formation factor as a function of porosity from laboratory measurements and micro-CT scan images from 2 sand samples of Scarborough and Cottesloe beaches of Perth basin, for fastest method of obtaining the formation factor from CT-scan images that takes shorter time (5-7 hours) with calculation from laboratory measurements that takes much more longer time (30-65days).

This approach is practical, easily repeatable in real time (though expensive) and can be an alternative method for calculating formation factor when time is not on the side of the experimenter, which is always the case. Results of images below 500^3 (Scarborough) and 350^3 (Cottesloe) beaches indicates that they are not suitable REV for pore scale networks.

In this paper, micro CT-scan images computational technique was employed to calculate properties such as porosity and formation factor on large three-dimensional digitized images of sand sample. We demonstrated that for most of the parameters studied here, the values obtained by computing micro CT-scan images agreed with the classical laboratory measurements and results from other workers. **"**This work was focused on establishing a robust methodology and workflow and we thus started with one of the most simple materials, though still highly relevant for many applications in oil & gas or water management environments. For more complex geological materials, such as low-permeability rocks, multi-mineralitic rocks, materials with conductive minerals, etc., further developments are obviously needed. However these developments are mostly related to the employed techniques (e.g. a higher-resolution imaging technique would be need for low-permeability rocks, a more complex laboratory set-up and techniques for measurements of rocks with conductive minerals or minerals with a non-negligible surface conductivity, etc.) rather to the overall workflow established here (comparison between laboratory and computed data through trends between properties) that remain valid."

Acknowledgments: We thank Dominic Howman, and Dr. Vassili Mikhaltsevitch for help in cell design and laboratory experiments and Dr. Andrew Squelch for help with image processing.

References

Adler, P., Jacquin, C., and Quiblier, J.: Flow in simulated porous media, International Journal of Multiphase Flow, 16, 691-712, 1990.

Adler, P. M., Jacquin, C. G., and Thovert, J. F.: The formation factor of reconstructed porous media, Water Resources Research, 28, 1571-1576, 1992.

Andrä, H., Combaret, N., Dvorkin, J., Glatt, E., Han, J., Kabel, M., Keehm, Y., Krzikalla, F., Lee, M., and Madonna, C.: Digital rock physics benchmarks—Part II: Computing effective properties, Computers & Geosciences, 50, 33-43, 2013a.

Andrä, H., Combaret, N., Dvorkin, J., Glatt, E., Han, J., Kabel, M., Keehm, Y., Krzikalla, F., Lee, M., and Madonna, C.: Digital rock physics benchmarks—Part I: Imaging and segmentation, Computers & Geosciences, 50, 25-32, 2013b.

Arns, C. H., Knackstedt, M. A., Pinczewski, W. V., and Mecke, K. R.: Euler-Poincaré characteristics of classes of disordered media, Physical Review E, 63, 031112, 2001.

Auzerais, F., Dunsmuir, J., Ferreol, B., Martys, N., Olson, J., Ramakrishnan, T., Rothman, D., and Schwartz, L.: Transport in sandstone: a study based on three dimensional microtomography, Geophysical Research Letters, 23, 705-708, 1996.

Bentz, D. P., and Martys, N. S.: Hydraulic radius and transport in reconstructed model three-dimensional porous media, Transport in porous media, 17, 221-238, 1994.

Constable, S., and Srnka, L. J.: An introduction to marine controlled-source electromagnetic methods for hydrocarbon exploration, Geophysics, 72, WA3-WA12, 2007.

Dunsmuir, J., Ferguson, S., and D'Amico, K.: Design and operation of an imaging X-ray detector for microtomography, Photoelectric Image Devices, the McGee Symposium, 1991, 257-264,

Dvorkin, J., Derzhi, N., Diaz, E., and Fang, Q.: Relevance of computational rock physics, Geophysics, 76, E141-E153, 2011.

Fredrich, J., Menendez, B., and Wong, T.: Imaging the pore structure of geomaterials, Science, 268, 276, 1995.

Guéguen, Y., and Palciauskas, V.: Introduction to the physics of rocks, Princeton University Press, 1994.

Jinguuji, M., Toprak, S., and Kunimatsu, S.: Visualization technique for liquefaction process in chamber experiments by using electrical resistivity monitoring, Soil Dynamics and Earthquake Engineering, 27, 191-199, 2007.

Joshi, M. Y.: A class of stochastic models for porous media, University of Kansas, 1974.

Miller, M. N.: Bounds for effective electrical, thermal, and magnetic properties of heterogeneous materials, Journal of Mathematical Physics, 10, 1988-2004, 1969.

Miller, R. L., Bradford, W. L., and Peters, N. E.: Specific conductance: theoretical considerations and application to analytical quality control, US Government Printing Office, 1988.

Milton, G. W.: Bounds on the elastic and transport properties of two-component composites, Journal of the Mechanics and Physics of Solids, 30, 177-191, 1982.

Mitsuhata, Y., Uchida, T., Matsuo, K., Marui, A., and Kusunose, K.: Various-scale electromagnetic investigations of high-salinity zones in a coastal plain, Geophysics, 71, B167-B173, 2006.

Nakashima, Y., and Nakano, T.: Accuracy of formation factors for three-dimensional pore-scale images of geo-materials estimated by renormalization technique, Journal of applied geophysics, 75, 31-41, 2011.

Øren, P.-E., and Bakke, S.: Process based reconstruction of sandstones and prediction of transport properties, Transport in Porous Media, 46, 311-343, 2002.

Øren, P. E., Bakke, S., and Held, R.: Direct pore-scale computation of material and transport properties for North Sea reservoir rocks, Water resources research, 43, 2007.

Schwartz, L., Auzerais, F., Dunsmuir, J., Martys, N., Bentz, D., and Torquato, S.: Transport and diffusion in three-dimensional composite media, Physica A: Statistical Mechanics and its Applications, 207, 28-36, 1994.

Spanne, P., Thovert, J., Jacquin, C., Lindquist, W., Jones, K., and Adler, P.: Synchrotron computed microtomography of porous media: topology and transports, Physical Review Letters, 73, 2001, 1994.

Torquato, S.: Thermal conductivity of disordered heterogeneous media from the microstructure, Reviews in Chemical Engineering, 4, 151-204, 1987.

Yeong, C., and Torquato, S.: Reconstructing random media, Physical Review E, 57, 495, 1998.

Zhan, X., and Toksoz, M. N.: Effective Conductivity Modeling of a Fluid Saturated Porous Rock, Massachusetts Institute of Technology. Earth Resources Laboratory, 2007.

545